





Protruding Pt single-sites on hexagonal ZnIn_2S_4 to accelerate photocatalytic hydrogen evolution

Xiaowei Shi¹, Chao Dai¹, Xin Wang¹, Jiayue Hu², Junying Zhang ³, Lingxia Zheng¹, Liang Mao ⁴✉, Huajun Zheng ¹✉ & Mingshan Zhu ²✉

Single-site cocatalysts engineered on supports offer a cost-efficient pathway to utilize precious metals, yet improving the performance further with minimal catalyst loading is still highly desirable. Here we have conducted a photochemical reaction to stabilize ultralow Pt co-catalysts (0.26 wt%) onto the basal plane of hexagonal ZnIn_2S_4 nanosheets ($\text{Pt}_{\text{SS}}\text{-ZIS}$) to form a Pt-S_3 protrusion tetrahedron coordination structure. Compared with the traditional defect-trapped Pt single-site counterparts, the protruding Pt single-sites on h -ZIS photocatalyst enhance the H_2 evolution yield rate by a factor of 2.2, which could reach $17.5 \text{ mmol g}^{-1} \text{ h}^{-1}$ under visible light irradiation. Importantly, through simple drop-casting, a thin $\text{Pt}_{\text{SS}}\text{-ZIS}$ film is prepared, and large amount of observable H_2 bubbles are generated, providing great potential for practical solar-light-driven H_2 production. The protruding single Pt atoms in $\text{Pt}_{\text{SS}}\text{-ZIS}$ could inhibit the recombination of electron-hole pairs and cause a tip effect to optimize the adsorption/desorption behavior of H through effective proton mass transfer, which synergistically promote reaction thermodynamics and kinetics.

¹Department of Applied Chemistry, Zhejiang University of Technology, 310032 Hangzhou, P.R. China. ²Guangdong Key Laboratory of Environmental Pollution and Health, School of Environment, Jinan University, 511443 Guangzhou, P.R. China. ³School of Physics, Beihang University, 100191 Beijing, P.R. China. ⁴School of Materials Science and Physics, China University of Mining and Technology, 221116 Xuzhou, P.R. China. ✉email: maoliang@cumt.edu.cn; zhenghj@zjut.edu.cn; zhumingshan@jnu.edu.cn

Water splitting for hydrogen (H_2) generation through solar light has attracted increasing attention since it supplies a significant carbon-neutral technology for zero-emission renewable energy evolution. The design of a photocatalyst with high efficiency and long durability is a focused task for researchers to scale up H_2 evolution reaction (HER) in the past decades¹. Two-dimensional (2D) hexagonal $ZnIn_2S_4$ (h -ZIS), a typical ternary chalcogenide with favorable H adsorption features at edge S atom in (110) facet ($\Delta G_H^* = -0.16$ eV) and robust resistance to photocorrosion, has been regarded as a promising candidate for photocatalytic water splitting^{2–6}. The current guiding principles for advancing the catalytic performance of h -ZIS are as follows. First, increase the active site density in h -ZIS through preferentially exposing the edge sites^{6,7}. Unfortunately, unleashing the intrinsically high activity of h -ZIS is still retarded by the severe recombination of electron-hole pairs, where only a small quantity of electrons could survive at the active sites. Second, create in-plane sulfur vacancies or dope metallic heteroatoms to substitute Zn atoms^{7–10}. The lifetime of photoexcited electrons is prolonged, and the basal-plane S atoms in those h -ZIS are also stimulated as centers for HER; however, these S sites suffer from less favorable hydrogen adsorption features ($\Delta G_H^* = -0.25$ eV) despite the increased site density⁹. Apparently, h -ZIS only becomes applicable toward photocatalytic HER when the rapid carrier recombination and limited active site obstacles are simultaneously overcome.

As a lamellar material, the basal plane of h -ZIS provides plenty of platforms for noble-metal nanoparticles loading, especially platinum (Pt), while the scarcity and high cost of the noble-metal co-catalysts tremendously inhibit their large-scale implementation^{2,11–13}. Alternatively, single-site co-catalysts (SSCs) emerge as a frontier for catalysis science due to their high atom efficiency and outstanding activity^{14,15}. The strong metal-support interaction caused by metal atoms and coordinated atoms would affect the charge distributions and introduce the electronic structure modifications, which influence the electron-hole pairs recombination and the adsorption behavior during the catalytic process, and eventually change their catalytic activity and selectivity^{16–19}. One of the effective strategies for advanced SSCs is to produce more active sites through increasing metal loading with no aggregation, and accordingly, several Pt single-site (Pt_{SS})-based photocatalysts (Pt loading with 8.7 wt%²⁰ or 12.0 wt%²¹) have exhibited exciting H_2 evolution rate and observable bubbles under visible light irradiation. For practical applications, achieving maximum catalytic performance with minimal noble-metal atoms is essentially required. Recently, Pt SSCs supported on highly curved substrates were successfully prepared as electrocatalyst to mimic the metal sites at the edges and corners of particles²². Owing to the accumulation of electrons around Pt regions triggered by the tip effect, an accelerated HER kinetics was achieved. Principally, the generation of tip enhancement is biased onto curvature-rich configurations (typically corner, vertex, or protrusion)²³. To this end, direct anchoring Pt SSCs onto h -ZIS nanosheets might be an effective approach to form tridimensional protrusion that could produce high- and cost-efficient photocatalysts for HER.

In this work, a photochemical route was employed to synthesize h -ZIS with Pt single sites (Pt_{SS} -ZIS)²⁴. The light-induced reaction is more moderate and controllable than traditional annealing methods, so the structure of h -ZIS could be well preserved without generating any vacancy defects. During photochemical processes, $PtCl_6^{2-}$ ions were reduced and concurrently immobilized on the basal plane of h -ZIS nanosheets, forming Pt-S₃ tetrahedron coordination structure with surrounding S atoms. Experiments and simulations jointly manifest that the atomically dispersed Pt atoms could serve as sinks to facilitate the separation of photoexcited electron-hole pairs as well as active centers to enhance the HER performance through the

accelerating catalytic kinetics. As a result, the synergetic effect of atomic-level Pt and h -ZIS produces a higher photocatalytic activity for H_2 evolution, where the activity outperforms that of defect-trapped Pt single-site counterpart. In addition, a thin film of Pt_{SS} -ZIS on the solid substrate could readily be achieved through a drop-casting approach, and a large amount of H_2 bubbles are generated during light irradiation (Supplementary Movies 1 and 2).

Results

Structure analysis and characterization. Ultrathin h -ZIS nanosheets with thickness ranging from 2.46 to 4.94 nm were prepared by a hydrothermal method (Supplementary Fig. 1)⁹. H_2PtCl_6 aqueous solution was introduced into h -ZIS dispersion with magnetic stirring. The interfacial charges of h -ZIS and Pt species ($HPtCl_6^-$ or $PtCl_6^{2-}$) were opposite, so they would be spontaneously assembled through electrostatic interaction in the solution, with Pt-ZIS mixture generated (Supplementary Fig. 2). After irradiation under visible light for 60 min, Pt sites were immobilized on h -ZIS, and the mixture was centrifuged and collected (see the Experimental Section and Supplementary Fig. 3). By alerting the volume of added H_2PtCl_6 , Pt loading content could be tuned, as quantified by the inductively coupled plasma optical emission spectroscopy (ICP-OES) analysis (Supplementary Table 1). Additionally, the molar ratio of Zn and In in $Pt_{0.3}$ -ZIS was calculated to be 0.225:0.451, which is consistent with the theoretical molar ratio of 1:2.

X-ray diffraction (XRD) patterns and Raman spectra with negligible changes are observed between h -ZIS and Pt-ZIS, suggesting that Pt atoms incorporation does not destroy the crystal structure of h -ZIS (Supplementary Fig. 4). Transmission electron microscopy (TEM) and high-resolution TEM (HRTEM) images in Supplementary Fig. 5 depict a sheet-like structure of h -ZIS and the lattice fringe of 0.41 nm corresponds to the (006) facet. After Pt deposition, the obtained Pt-ZIS nanosheets maintain the thickness (3.10–5.11 nm) of pristine h -ZIS recorded by atomic force microscope (AFM) (Supplementary Figs. 6 and 7). As shown in TEM and HRTEM images, no Pt nanoparticles are observed with Pt loading content in the range of 0.1–1.4 wt%, and the energy-dispersive X-ray spectroscopy (EDS) also exhibits homogeneous dispersion of Pt on h -ZIS nanosheets without any aggregation (Fig. 1a–d and Supplementary Figs. 8–10). When further increasing the Pt amount to 3.0 wt%, nanoparticles were formed, which is proved by the green circles and corresponding EDS spectrum (Supplementary Fig. 11). In addition, the lattice fringe of 0.293 and 0.196 nm attribute to the h -ZIS (104) and Pt (200) facet, respectively. To reveal the configuration of Pt co-catalyst on h -ZIS nanosheets, aberration-corrected high angle annular dark field STEM (HAADF-STEM) measurements were carried out on h -ZIS and $Pt_{0.3}$ -ZIS. Since the contrast in HAADF-STEM image is proportional to the square of atomic number, Pt is much brighter than Zn, In, and S atoms, and the atomically dispersed bright spots (circled) in Fig. 1e and Supplementary Fig. 12 confirm the formation of single Pt atoms²⁵. On the contrary, no bright spots could be observed in h -ZIS, and the cross-sectional profiles of atom contrast show almost identical intensity (Supplementary Fig. 13). As a result, the cross-sectional intensity in Fig. 1f and g, together with the ICP-OES results and electron spin resonance (ESR) spectra (Supplementary Fig. 14), directly identify that Pt SSCs exist, not as interior dopants substituting for Zn or In in h -ZIS skeletons, but as external adatoms conjugating with h -ZIS to engender tridimensional protrusions, different from extensively reported planar geometry of metal-N_x- and defect-trapped-SSCs^{13,26}. To illustrate the exact position of Pt single sites, density functional theory (DFT)

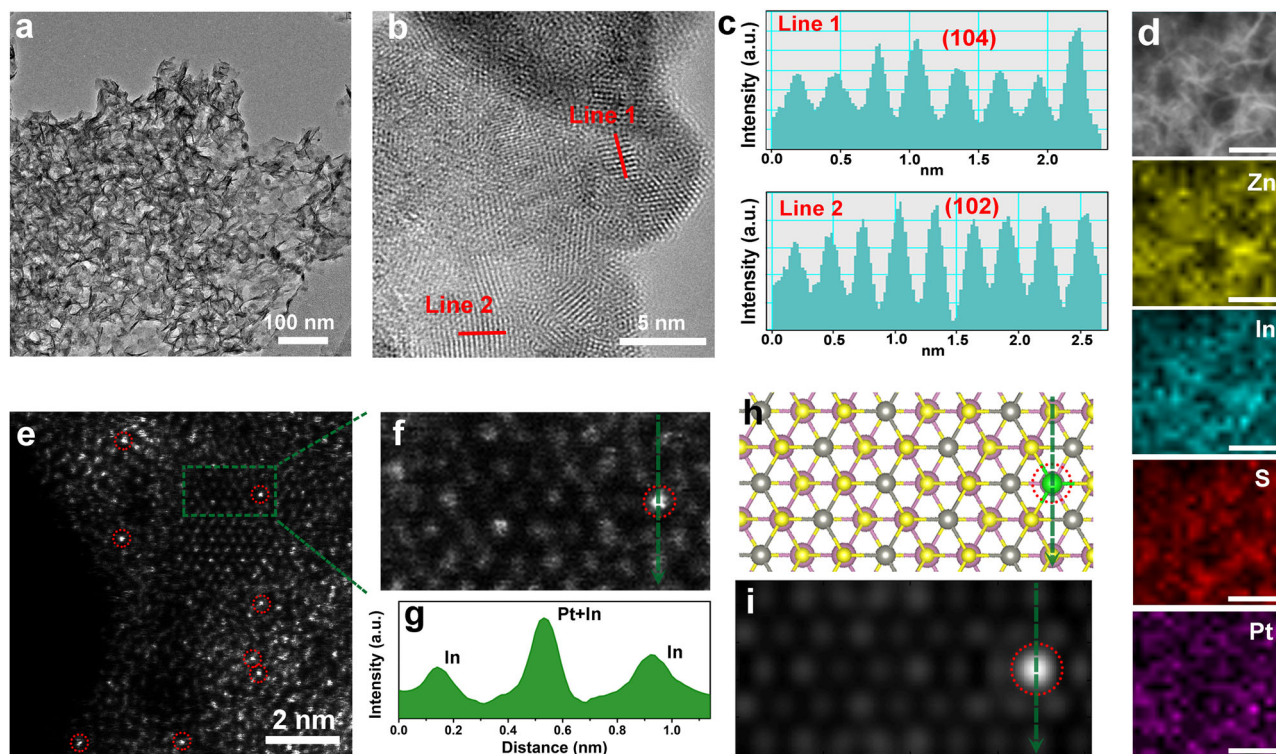


Fig. 1 Structural characterization of $\text{Pt}_{0.3}\text{-ZIS}$. **a** TEM image of $\text{Pt}_{0.3}\text{-ZIS}$. **b, c** HRTEM image of $\text{Pt}_{0.3}\text{-ZIS}$. **d** Elemental mapping of $\text{Pt}_{0.3}\text{-ZIS}$. The scale bars are 50 nm. **e** HAADF-STEM image of $\text{Pt}_{0.3}\text{-ZIS}$. **f** Magnified HAADF-STEM image of $\text{Pt}_{0.3}\text{-ZIS}$. **g** Strength profiles from the areas labeled by green line. **h** Optimized structure of $\text{Pt}_{0.3}\text{-ZIS}$. The yellow, gray, pink, and green spheres represent the S, Zn, In, and Pt atom, respectively. **i** Simulated HAADF-STEM image of $\text{Pt}_{0.3}\text{-ZIS}$ according to DFT-optimized structure.

calculations were carried out to determine the energies of Pt atoms on various sites. Six different locations were established, including Zn-S hollow site, Zn atop, S atop on Zn-S plane, In-S hollow site, In atop, and S atop on In-S plane, respectively, and Zn-S hollow site with the largest adsorption energy is confirmed to be the most stable location for Pt atom occupation (Supplementary Figs. 15–17). The distribution of Pt atoms on *h*-ZIS and their propensity to agglomerate was also examined by calculating the energy difference between an isolated Pt atom and a Pt dimer (ΔE_d), in which the total energy of the isolated configuration was used as reference energy. As shown in Supplementary Fig. 18, it is more favorable for the Pt atoms to be isolated at Zn-S hollow site due to the positive ΔE_d of 2.03 eV, which fully supports the experimental observations of the Pt single atom in $\text{Pt}_{0.3}\text{-ZIS}$. Based on the DFT-optimized structure, a STEM simulation on Pt SSCs dispersed *h*-ZIS was performed. The simulated result is in good agreement with the experimental HAADF-STEM image, demonstrating that Pt single sites prefer to chemisorb above the Zn-S hollow site in *h*-ZIS basal plane (Fig. 1h and i).

Electronic states of atoms in Pt-ZIS. Elemental composition and chemical states of Pt-ZIS were characterized by X-ray photoelectron spectroscopy (XPS). The high-resolution Zn 2p and In 3d XPS peaks corresponding to *h*-ZIS, $\text{Pt}_{0.3}\text{-ZIS}$, and $\text{Pt}_{3.0}\text{-ZIS}$ exhibit little shift (Supplementary Fig. 19). The S 2p spectrum for *h*-ZIS shows two peaks at 161.8 and 163.0 eV, respectively. After loading Pt single sites, a blue-shift of ~ 0.4 eV in $\text{Pt}_{0.3}\text{-ZIS}$ is observed, indicating that the electrons are transferred from Pt to *h*-ZIS and enriched around S atom. This also proves that the decoration of Pt single atoms would modulate the electronic structures of *h*-ZIS (Fig. 2a)^{20,27}. With the increasing amount of Pt to 3.0 wt%, a smaller blue-shift of about 0.3 eV is detected. For

the Pt 4f spectra, Pt/C exhibits three peaks at 71.90, 71.77, and 73.19 eV, which correspond to the Pt^0 , Pt^{2+} , and Pt^{4+} state, respectively (Fig. 2b)¹⁶. In contrast, the $\text{Pt}_{0.3}\text{-ZIS}$ mainly contains $\text{Pt}^{\delta+}$ species (72.10 eV), revealing the formation of a higher coordination number with the Pt–S bonds than the Pt–Pt bonds^{28–30}. Interestingly, both Pt^0 and $\text{Pt}^{\delta+}$ peaks appear in the spectrum of $\text{Pt}_{3.0}\text{-ZIS}$ (70.90 and 72.09 eV), which is probably owing to the well-constructed both Pt single atoms and nanoparticles²⁹. The detailed information for XPS fits is listed in Supplementary Tables 2–5.

Furthermore, X-ray absorption near-edge structure (XANES) and extended X-ray absorption fine structure spectroscopy (EXAFS) were conducted to investigate the local atomic structure and electronic environment of Pt species in Pt-ZIS. EXAFS results in Fig. 2c show k^2 -weighted Fourier transforms from the Pt L₃-edge EXAFS oscillations of $\text{Pt}_{1.4}\text{-ZIS}$ and $\text{Pt}_{3.0}\text{-ZIS}$ in comparison to that of Pt foil and PtO_2 (k^2 -weighted $\chi(k)$ signals in Supplementary Fig. 20). The only prominent shell in $\text{Pt}_{1.4}\text{-ZIS}$ locating at near 2.0 Å without any Pt–Pt contribution in the range of 2–3 Å testifies the atomically dispersed Pt on *h*-ZIS^{17,29}, whereas an additional peak at about 2.6 Å arises in $\text{Pt}_{3.0}\text{-ZIS}$, closing to that of Pt–Pt contribution. To gain visual illustrations of Pt coordination conditions, wavelet transform (WT) of the k^2 -weighted EXAFS spectra, a reflection of structure information in the resolution of *R* space and *K* space, are shown in Fig. 2d. $\text{Pt}_{1.4}\text{-ZIS}$ exhibits the maximum WT intensity at 1.8–2.1 Å in *R* space and 3–6 Å in *k* space, ascribing to Pt–S bond in the first coordination shell^{31,32}. While a new WT intensity maximum near 2.5–2.8 Å and 9–11 Å suggests the coexistence of Pt–S and Pt–Pt bonds in $\text{Pt}_{3.0}\text{-ZIS}$. The Fourier-transform EXAFS curves and the corresponding fitting results in Supplementary Fig. 21 and Supplementary Table 6 give the Pt–S coordination number of 2.6 for $\text{Pt}_{1.4}\text{-ZIS}$, implying a similar coordination condition of

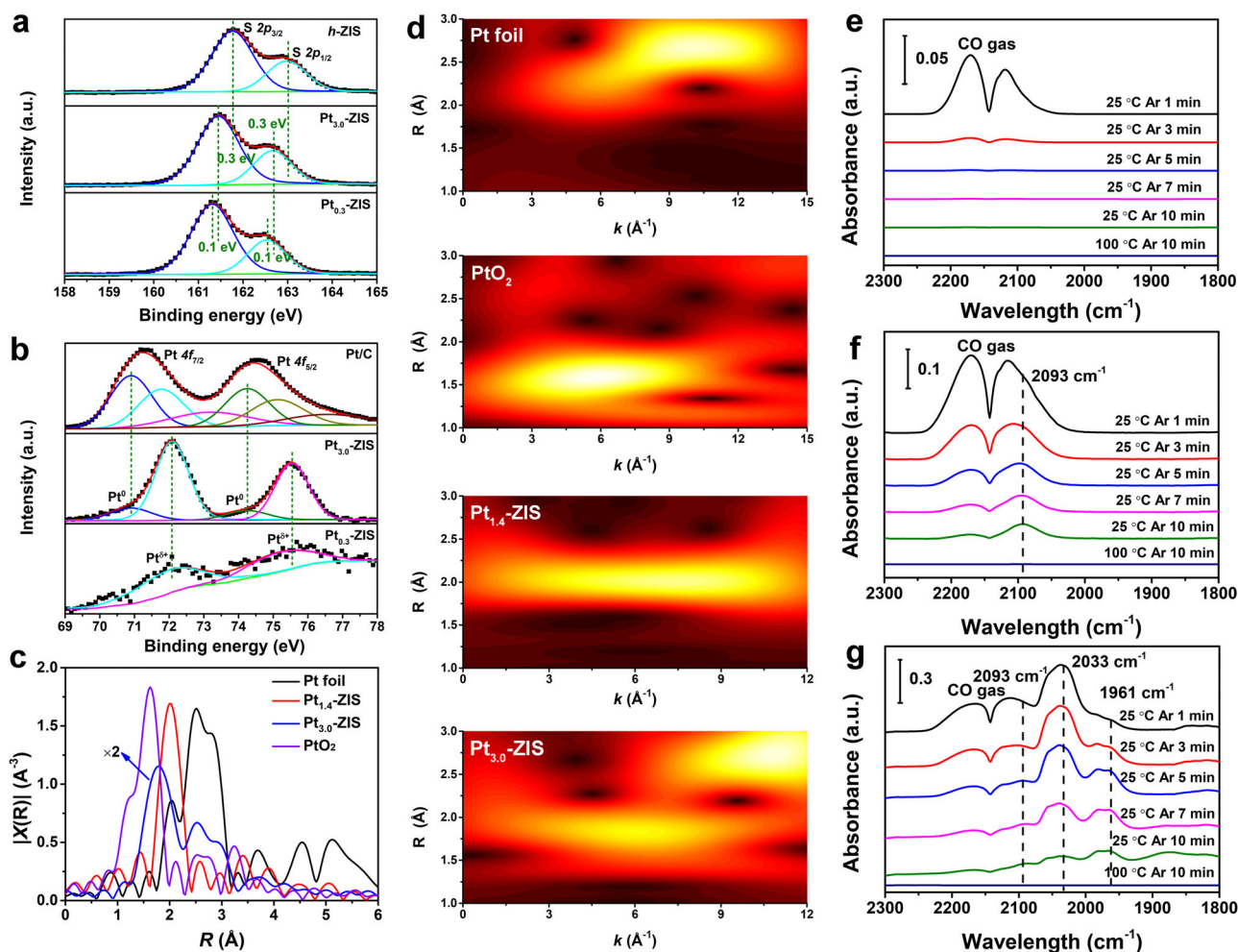


Fig. 2 Electronic states of atoms in photocatalysts. **a** High-resolution XPS spectra (S 2p) of *h*-ZIS, Pt_{3.0}-ZIS, and Pt_{0.3}-ZIS. **b** High-resolution XPS spectra (Pt 4f) of Pt/C, Pt_{3.0}-ZIS, and Pt_{0.3}-ZIS. **c** Fourier transform of k^2 -weighted Pt L₃-edge of the EXAFS spectra for Pt foil, PtO₂, Pt_{1.4}-ZIS, and Pt_{3.0}-ZIS. **d** Wavelet transform for the k^2 -weighted EXAFS spectra of Pt foil, PtO₂, Pt_{1.4}-ZIS, and Pt_{3.0}-ZIS. *R* is the interatomic distance. FTIR spectra of CO adsorbed after the desorption processes for **e** *h*-ZIS, **f** Pt_{0.3}-ZIS, and **g** Pt_{3.0}-ZIS.

Pt–S₃ in Pt_{SS}-ZIS as depicted by HAADF-STEM image and DFT simulations. The XANES spectra of Pt L₃-edge show that the white-line intensity of Pt_{1.4}-ZIS is lower than that of PtO₂, but higher than that of Pt_{3.0}-ZIS and Pt foil, demonstrating the Pt atoms are in an oxidation state originating from covalent Pt–S bonds, which is consistent with XPS results (Supplementary Fig. 22)¹⁹.

Moreover, we investigated the CO adsorption behavior on different photocatalysts using Fourier-transform infrared (FTIR) spectroscopy to provide additional information about the dispersion and chemical state of Pt (Fig. 2e–g). For Pt_{0.3}-ZIS, only a weak vibration band appears at 2093 cm^{−1} corresponding to CO adsorption on Pt^{δ+}^{33,34}. While the adsorption of CO also produces a strong vibration band at 2033 cm^{−1} and another weak band at 1961 cm^{−1} for Pt_{3.0}-ZIS. The main band at 2033 cm^{−1} can be ascribed to linearly bonded CO on Pt⁰ sites, and the band at 1961 cm^{−1} is caused by CO adsorbed on the interface between Pt clusters and the support³³. All these characterizations provide compelling evidence that our protocol affords Pt_{0.3}-ZIS with only positively charged Pt single atoms, while Pt_{3.0}-ZIS with both single atoms and Pt nanoparticles.

Photocatalytic H₂ evolution performances. With protrusion-shaped SSCs in hand, we next explored their photocatalytic HER

activities in an aqueous solution with 10 vol% triethanolamine (TEOA) as the sacrificial agent under visible light ($\lambda > 420$ nm) irradiation. According to Fig. 3a, all Pt-loaded *h*-ZIS photocatalysts exhibit higher H₂ evolution performance than the counterpart (*h*-ZIS: 19.67 $\mu\text{mol h}^{-1}$ with 20 mg photocatalyst). The optimized rate (350.1 $\mu\text{mol h}^{-1}$) is acquired at Pt_{0.3}-ZIS, which is about 17.8 times enhanced than that of pristine *h*-ZIS. When Pt loading content exceeds 0.3 wt%, the activity experiences a decrease, and the catalytic efficiency of each Pt site is reduced (Supplementary Fig. 23). In addition, *h*-ZIS with sulfur vacancies (*h*-ZIS-V_S) was synthesized through the treatment of NaBH₄ in a water bath. Benefiting from the existence of localized states caused by sulfur vacancies, *h*-ZIS-V_S performs a narrower bandgap (2.66 eV) and a longer average fluorescence lifetime (5.86 ns) than *h*-ZIS (2.79 eV and 3.02 ns) (Supplementary Figs. 24 and 25). As a result, the photocatalytic activity of *h*-ZIS is enhanced after creating sulfur vacancies. Then Pt_{0.3}-ZIS-V_S (0.28 wt% Pt) was also prepared by the same photochemical procedure (Supplementary Fig. 26). The obviously decreased ESR signal of Pt_{0.3}-ZIS-V_S and the calculated adsorption energy reveal that Pt single atoms incline to be trapped at defect sites rather than protrude out of *h*-ZIS-V_S surface (Supplementary Figs. 26, 27). The recorded H₂ generation rate for Pt_{0.3}-ZIS-V_S is only about half of that for Pt_{0.3}-ZIS (Fig. 3b). These results imply that the excellent catalytic activity of Pt_{0.3}-ZIS could be mainly

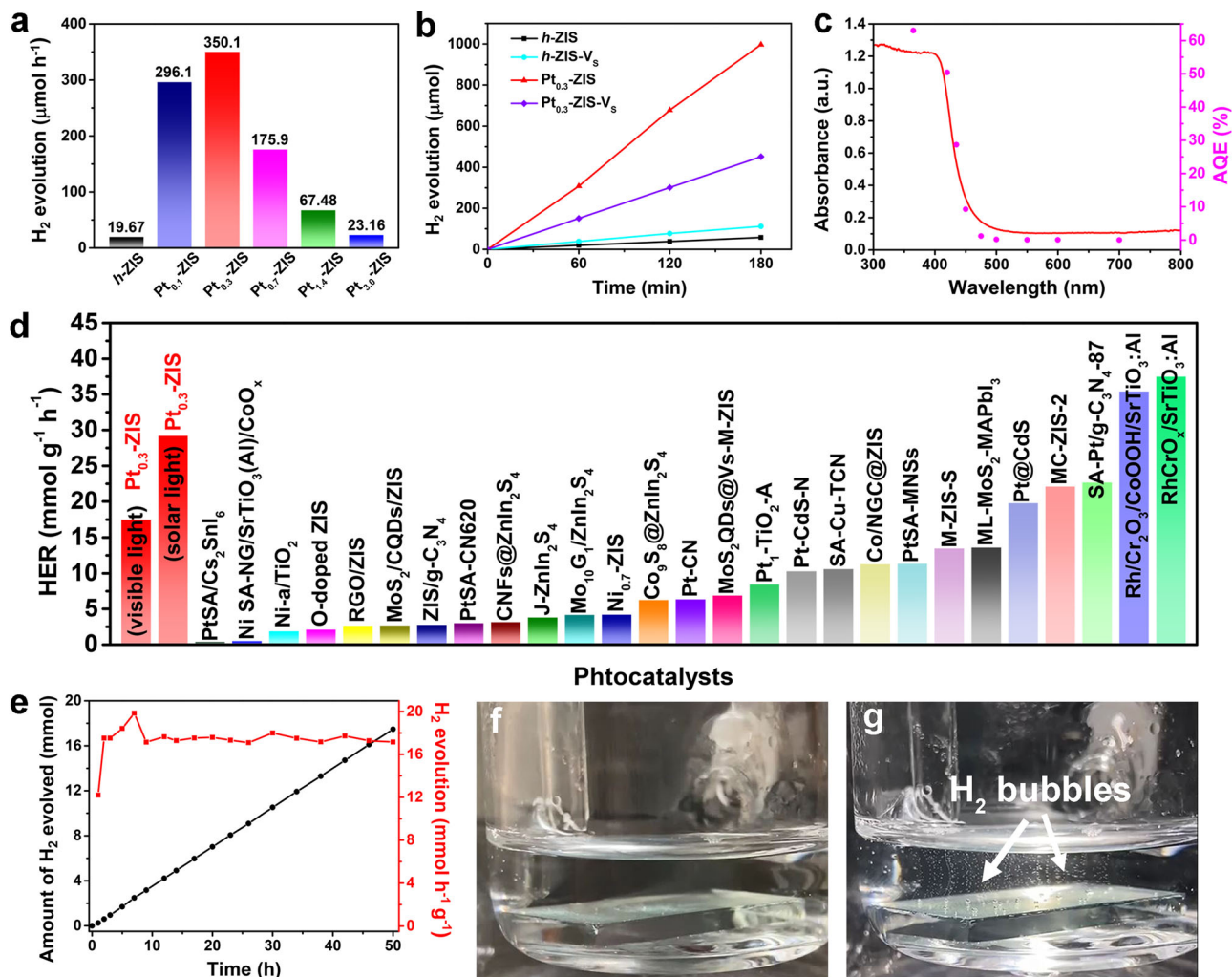


Fig. 3 Evaluation of photocatalytic HER performances. **a** Visible light ($\lambda > 420$ nm) photocatalytic H₂ evolution activities of *h*-ZIS and Pt-ZIS with different Pt loading content. **b** Visible light ($\lambda > 420$ nm) photocatalytic H₂ evolution activity of Pt_{0.3}-ZIS in comparison with *h*-ZIS, *h*-ZIS-V_s, and Pt_{0.3}-ZIS-V_s. **c** Wavelength dependence of the AQE for Pt_{0.3}-ZIS. **d** H₂ evolution rates for Pt_{0.3}-ZIS in this work compared with representative recently reported photocatalysts. **e** Cycling stability test of Pt_{0.3}-ZIS. **f, g** Digital photograph of H₂ evolution using Pt_{0.3}-ZIS film without and with visible light irradiation.

attributed to the protrusion-like Pt species on 2D *h*-ZIS. Similar to the trend of visible light, Pt_{0.3}-ZIS also displays a boosted activity under simulated solar light with a total H₂ generation of 3504 μmol within 6 h, whereas only 245.7 μmol H₂ is formed by *h*-ZIS (Supplementary Fig. 28). Additionally, Pt_{0.3}-ZIS could introduce acceptable HER performance even in pure water and the H₂ evolution rate is ~24.04 μmol h⁻¹ (1202 μmol h⁻¹ g⁻¹) under visible light irradiation (Supplementary Fig. 29). Dependence of apparent quantum efficiency (AQE) at each wavelength for Pt_{0.3}-ZIS derived from the amount of generated H₂ was estimated by various band-pass filters (Fig. 3c and Supplementary Table 7). The AQE matches well with the absorption spectrum of Pt_{0.3}-ZIS, and reaches up to 50.4% at 420 nm. Experiments in dark or without photocatalysts show no H₂ evolution, demonstrating that H₂ is generated by the photocatalysis processes. Such high AQE and catalytic HER activity of Pt_{0.3}-ZIS is far beyond the majority of representative photocatalysts (details see the comparisons in Fig. 3d and Supplementary Table 8). Furthermore, Pt_{0.3}-ZIS almost maintains its photocatalytic H₂ evolution rate at the initial level after continuous irradiation for 50 h (Fig. 3e). The characterizations including XRD, XPS, TEM, and HAADF-STEM, demonstrate that the structures undergo negligible

changes, manifesting high stability of Pt_{0.3}-ZIS (Supplementary Figs. 30–33).

Due to its outstanding performance, we dispersed Pt_{0.3}-ZIS into ethanol solution and then drop-casted onto FTO substrate (1.5 × 2 cm²) to form a thin film (~3 μm thick) with excellent transmittance (Supplementary Figs. 34 and 35). As a proof-of-concept, the resultant Pt_{0.3}-ZIS film was employed as a photocatalyst for H₂ production. No H₂ is generated before irradiation, while small H₂ bubbles start to appear continuously when turning on the light (Fig. 3f, g and Supplementary Movies 1, 2). The H₂ generation rate over the film achieves as high as 0.967 L h⁻¹ m⁻² (43.17 mmol h⁻¹ m⁻²) under visible light irradiation, outperforming numerous recent reported photocatalysis films, such as C₃N₄ film (0.19 L h⁻¹ m⁻²) and Pt₅₅-MOF (0.398 L h⁻¹ m⁻²), which dictates an enormous potential for real applications^{21,35}.

Insight of the increased photocatalytic activity. To shed light on the origin of enhanced activity, three elementary processes in photocatalysis HER, namely light absorption, charge separation, and interfacial H₂ catalysis, are taken into consideration. The optical absorption properties were examined by ultraviolet-visible

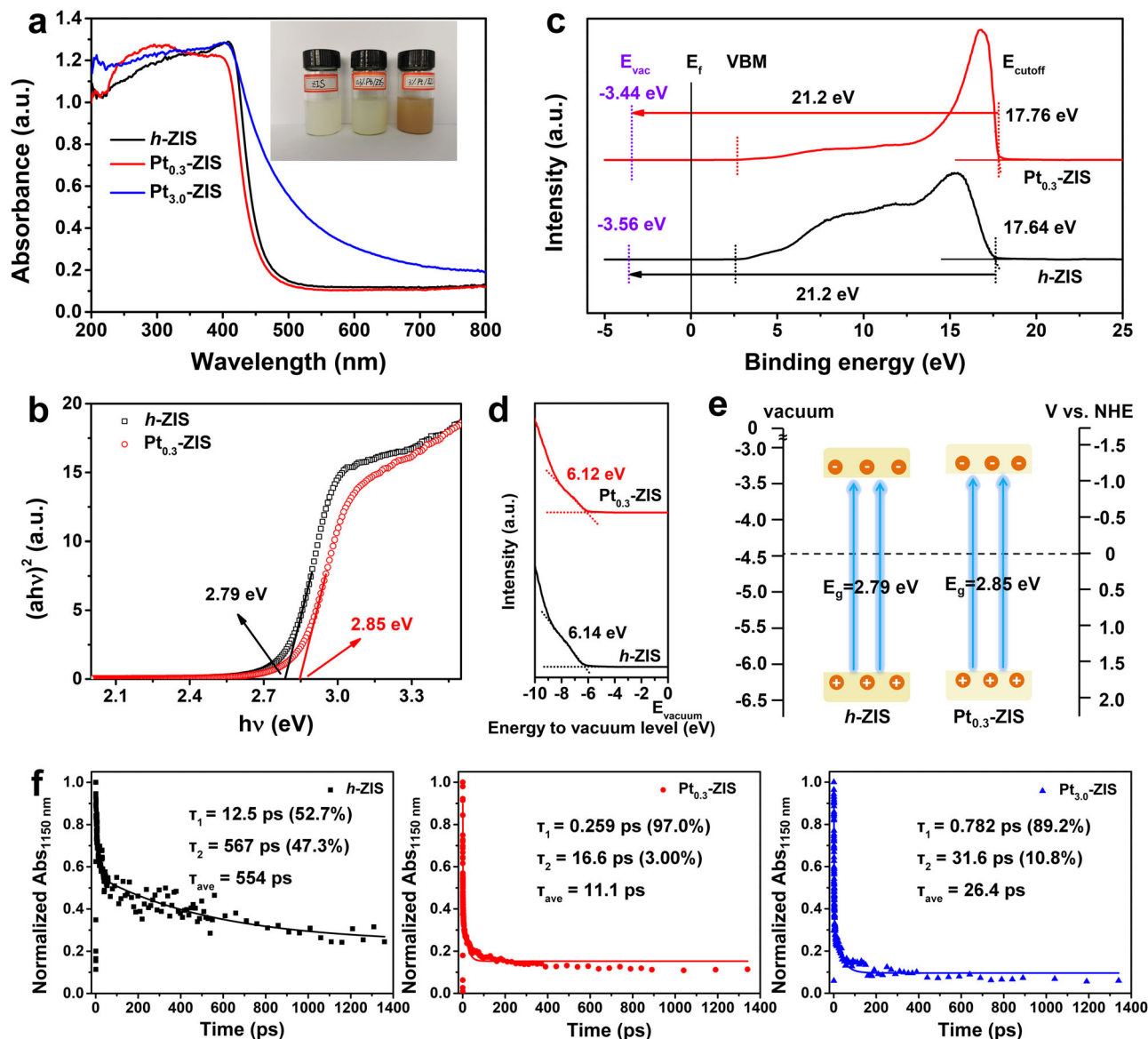


Fig. 4 Mechanism insight the photocatalytic H₂ evolution. **a** UV-vis diffuse reflectance spectra for *h*-ZIS, Pt_{0.3}-ZIS, and Pt_{3.0}-ZIS, insert: digital images for *h*-ZIS, Pt_{0.3}-ZIS, and Pt_{3.0}-ZIS, the concentration of suspensions is 2 mg mL⁻¹. **b** Bandgap for *h*-ZIS and Pt_{0.3}-ZIS. **c** Comparison and relationship of VBM, E_f, and E_{vac} of UPS spectra. **d** UPS spectra of *h*-ZIS and Pt_{0.3}-ZIS in the valence band region. **e** Schematic illustration of the band structure of *h*-ZIS and Pt_{0.3}-ZIS. **f** Normalized time profiles of transient absorption at 1150 nm during the TDR of *h*-ZIS, Pt_{0.3}-ZIS, and Pt_{3.0}-ZIS.

(UV-vis) diffuse reflectance spectra. An absorption edge at around 440 nm corresponding to the bandgap of about 2.85 eV, is observed for Pt_{0.3}-ZIS. It is slightly larger than that of pristine *h*-ZIS (2.79 eV), revealing a blue-shift absorption edge of *h*-ZIS upon Pt stabilizing (Fig. 4a and b). These results are similar to those achieved from the photocurrent action spectra of different photocatalysts film electrodes (Supplementary Fig. 36). Even though the light absorption is enhanced in the visible range with further increasing the amount of Pt (Pt_{3.0}-ZIS), the measured photocurrent action spectrum of Pt_{3.0}-ZIS is quite different from its UV-vis absorbance, in which there is almost no photocurrent at 500 nm. Additionally, the AQE of Pt_{3.0}-ZIS was also recorded (Supplementary Fig. 37 and Table S7). Consistent with the photocurrent action, the AQE of Pt_{3.0}-ZIS does not follow well with the UV-vis spectrum and only a little amount of H₂ is generated at 500 nm. Considering that the Pt colloids exhibit broadband optical absorption from ultraviolet to the visible light region, we can conclude that Pt nanoparticles formed in Pt_{3.0}-ZIS could

extend the light absorption, but have limited contributions to the photocatalytic performances of *h*-ZIS³⁶. The digital images demonstrate an obvious color change from ivory to pale yellow for *h*-ZIS and Pt_{0.3}-ZIS, and finally to dark brown for Pt_{3.0}-ZIS. The relationship between VBM, E_f, and E_{vac}, and the UPS spectra of different photocatalysts are shown in Fig. 4c. The vacuum level (E_{vac}) should be located 21.2 eV above the cutoff energy (E_{cutoff}) of the spectrum. The relative locations of valence band maximum (VBM) are calculated to be -6.14 eV (*h*-ZIS) and -6.12 eV (Pt_{0.3}-ZIS) compared with E_{vac} according to UPS spectra (Fig. 4d). As a result, *h*-ZIS and Pt_{0.3}-ZIS display the conduction band minimum (CBM) potential of -3.35 and -3.27 eV, respectively (Fig. 4e). The elevation of CBM endows the photoexcited electrons in Pt_{0.3}-ZIS with a higher reduction ability to react with hydrogen ions and form molecular hydrogen in HER compared with *h*-ZIS⁴. This favorable feature of the band structure is advantageous to prohibit the recombination of

electron-hole pairs, and is responsible for the enhanced photocatalytic performance of Pt_{0.3}-ZIS.

The electron dynamics involved in photocatalysis were revealed by time-resolved diffuse reflectance (TDR) spectroscopy, a robust technique to provide direct evidence for the effect of Pt loading on charge separation in semiconductors^{37,38}. The pump light with a central wavelength of 420 nm was used, which is effective for photoinduced an interband transition in *h*-ZIS. It turns out that probing in the wavelength range of 900–1200 nm yielded similar TDR spectra, featuring free or trapped photoexcited electrons (Supplementary Fig. 38)^{6,39,40}. And a set of representative data obtained at 1150 nm combined with the biexponential fitting results are illustrated. In Fig. 4f, the two-time constants for *h*-ZIS are $\tau_1 = 12.5$ ps (52.7%) and $\tau_2 = 567$ ps (47.3%), respectively, and the weighted average lifetime is 554 ps. In comparison, the characterized two-time constants for Pt_{0.3}-ZIS ($\tau_1 = 0.259$ ps (97.0%) and $\tau_2 = 16.6$ ps (3.0%)) and Pt_{3.0}-ZIS ($\tau_1 = 0.782$ ps (89.2%) and $\tau_2 = 31.6$ ps (10.8%)) lead to much shorter average lifetime of 11.1 and 26.4 ps, respectively. In general, the average recovery lifetime is considered as a crucial indicator for evaluating the separation efficiency of photoexcited electron-hole pairs, and such a shortened lifetime indicates the opening of an additional pathway for electron transfer after Pt deposition^{41,42}. Based on the mean transient decay times of *h*-ZIS (τ_{ZIS}), Pt_{0.3}-ZIS ($\tau_{0.3}$), and Pt_{3.0}-ZIS ($\tau_{3.0}$), we can determine the injection rate through the equation as $k_{ET} = (1/\tau_x) - (1/\tau_{ZIS})$, where x represents the weight ratio of Pt^{43,44}. It is calculated that the k_{ET} of Pt_{0.3}-ZIS is 8.8×10^7 s⁻¹, to be ~2.4 times faster than that of Pt_{3.0}-ZIS (3.6×10^7 s⁻¹). In addition, as a more significant parameter for photocatalytic activity, the efficiency of electron injection (η_{inj}) from *h*-ZIS to Pt is calculated as $\eta_{inj} = 1 - \tau_x/\tau_{ZIS}$ ^{43,44}, and Pt_{0.3}-ZIS affords a higher η_{inj} ($\eta_{inj} = 98.0\%$) than that of Pt_{3.0}-ZIS ($\eta_{inj} = 95.2\%$).

Additionally, steady-state photoluminescence (PL) spectra were recorded (Supplementary Fig. 39). Loading Pt onto *h*-ZIS results in significant PL quenching for Pt-ZIS, and Pt_{0.3}-ZIS exhibits the lowest PL intensity among the photocatalysts, demonstrating an improvement in charge separation⁴⁵. Concurrently, the photocurrent intensity of Pt_{0.3}-ZIS is around 6.5 and 3.9 times compared with that of *h*-ZIS and Pt_{3.0}-ZIS, respectively (Supplementary Fig. 40a). EIS Nyquist plots of *h*-ZIS, Pt_{0.3}-ZIS, and Pt_{3.0}-ZIS together with simulated equivalent electrical circuits are also provided in Supplementary Fig. 40b and c, respectively, in which R_{ct} is interfacial charge-transfer resistance⁴⁶. Based on the model, Pt_{0.3}-ZIS shows the smallest semicircle diameter and R_{ct} value (Supplementary Table 10), proving the lowest resistance of interfacial charge transfer in Pt_{0.3}-ZIS⁴⁷. The efficient charge separation in Pt_{0.3}-ZIS was also confirmed by photocatalytic activation of peroxydisulfate (PMS) to degrade antibiotic ornidazole (ONZ) pollutants (Supplementary Fig. 41). For Pt_{0.3}-ZIS, the degradation efficiency of ONZ is 1.8 and 1.7 times and the utilization efficiency of PMS is 2.4 and 1.8 times than *h*-ZIS and Pt_{3.0}-ZIS, respectively. The effective electrons injection from Pt_{0.3}-ZIS to PMS molecules generate more reactive species, contributing to the higher photocatalytic performance than *h*-ZIS and Pt_{3.0}-ZIS. These results disclose that more rapid and efficient directional migration of photogenerated electrons is realized by isolated Pt atoms decoration, partly accounting for Pt_{0.3}-ZIS with the greatly enhanced photocatalytic performance^{38,48}.

DFT calculations were further carried out to dive fundamental insight into the effect of atomical Pt decoration. The charge density difference isosurface images reveal a strong charge redistribution at Pt-bonding region after the presence of protrusion-like single Pt atom on the basal plane of *h*-ZIS, and the calculated Bader charge shows that 0.06 e is transferred from

Pt to S atoms in the *h*-ZIS substrate, confirming the strong interaction between Pt and *h*-ZIS (Fig. 5a and b)³⁰. It is also observed that the Pt–S₃ coordination has obvious charge transfer along the z direction. When the Pt adsorbate hybridizes with the p band of S, the adsorbate state split into localized bonding and antibonding states. In the projected density of states (PDOS) profile for Pt_{SS}-ZIS, the dominant feature is Pt 5d-S 3p bonding resonances below the Fermi level and forming hybridized electronic states (Fig. 5c). Such states are considered as the electron acceptor states that could endow Pt_{SS}-ZIS with metallic conductive character to inhibit the recombination of electron-hole pairs⁴⁹. Moreover, the antibonding states of Pt_{SS}-ZIS with the position all above the Fermi level involve in constructing conduction band, which probably leads to the upshift of CBM¹⁹. This enlarged bandgap for Pt_{SS}-ZIS is consistent with the UV-vis absorption spectra and UPS spectra. Hence, theoretical calculations suggest that the covalent Pt–S coordination bond within Pt_{SS}-ZIS forms additional charge-transfer channels to improve the charge mobility, causing an enhanced photocatalytic activity.

To disclose the underlying interfacial catalytic contribution of H₂O to H₂ from Pt single site, the adsorption of H atom on Pt atom was investigated. It is demonstrated that the adsorption strength of H decreases with an increase in the number of adsorbed H atoms, eventually leading to a minimum value when four H atoms are adsorbed (Fig. 5d). The single H atom exhibits adsorption energy (E_a) of 0.613 eV, while it decreases to 0.564 eV per H in the case of two H atoms. As the number of interacting H atoms increases, the Pt to H interaction for bond formation becomes a compromise between the H–H electrostatic repulsion and the orbital hybridization of Pt–H⁵⁰. Specifically, when three H atoms adsorb onto a single Pt atom, they locate symmetrically around Pt site, leading to corresponding adsorption energy of 0.543 eV per H. With the number of H atoms reaching four, the adsorption configuration is one in which a H₂ dimer and two isolated H atoms are formed with an adsorption energy of 0.436 eV per H (Fig. 5d and e). The bond length of Pt–3H is elongated from 1.551 to 1.746 Å, and that of Pt–4H is 1.723 Å, which are much longer than that of Pt–1H (1.567 Å) and Pt–2H (1.566 Å) (the detailed distance of H–H atoms and Pt–H atoms are labeled in Fig. 5d). Moreover, the distance between 3H and 4H is only 0.881 Å, close to that in H₂ molecule (0.740 Å). These phenomena indicate the weakened adsorption strength of 3H and 4H on Pt single site, thus promoting the desorption of 3H and 4H and ease of H₂ production on Pt atom.

Finally, we performed the H adsorption free energy (ΔG_H^*) to examine the HER activity for different sites and the number of H atoms. Our simulations indicate that the adsorbed H on Pt, neighboring S, neighboring Zn, and second-neighboring Zn move to the tilted top site toward adjacent Zn atom on the surface after relaxation with an identical ΔG_H^* of -0.36 eV, and the ΔG_H^* of second-neighboring S is 0.61 eV (Supplementary Figs. 42, 43, and Table 11). Furthermore, the ΔG_H^* gradually increases for the second (-0.26 eV) and third (-0.23 eV) adsorbed H atoms on Pt single site, and it becomes positive for the fourth adsorbed H atom ($+0.10$ eV) (Supplementary Fig. 44). Commonly, one material is regarded as a good HER catalyst when the value of ΔG_H^* is close to thermoneutral ($\Delta G_H^* \approx 0$)⁵¹. Therefore, we suggest that the Pt single atom would be the active site for HER and the catalyst that forms in situ states might be H_{3,ads}Pt-ZIS³¹. DFT simulations were also carried out on Pt_{SS}-ZIS-V_S. Unlike Pt_{SS}-ZIS, H atom tends to be adsorbed right above Pt atom after structural relaxation, suggesting that it is difficult for Pt atom in Pt_{SS}-ZIS-V_S to adsorb more H atom (Supplementary Fig. 45). Additionally, the calculated ΔG_H^* for H atom on Pt_{SS}-ZIS-V_S is -0.22 eV, which is larger than that of H_{3,ads}Pt_{SS}-ZIS ($+0.10$ eV). These results prove the recently reported tip enhancement effect that

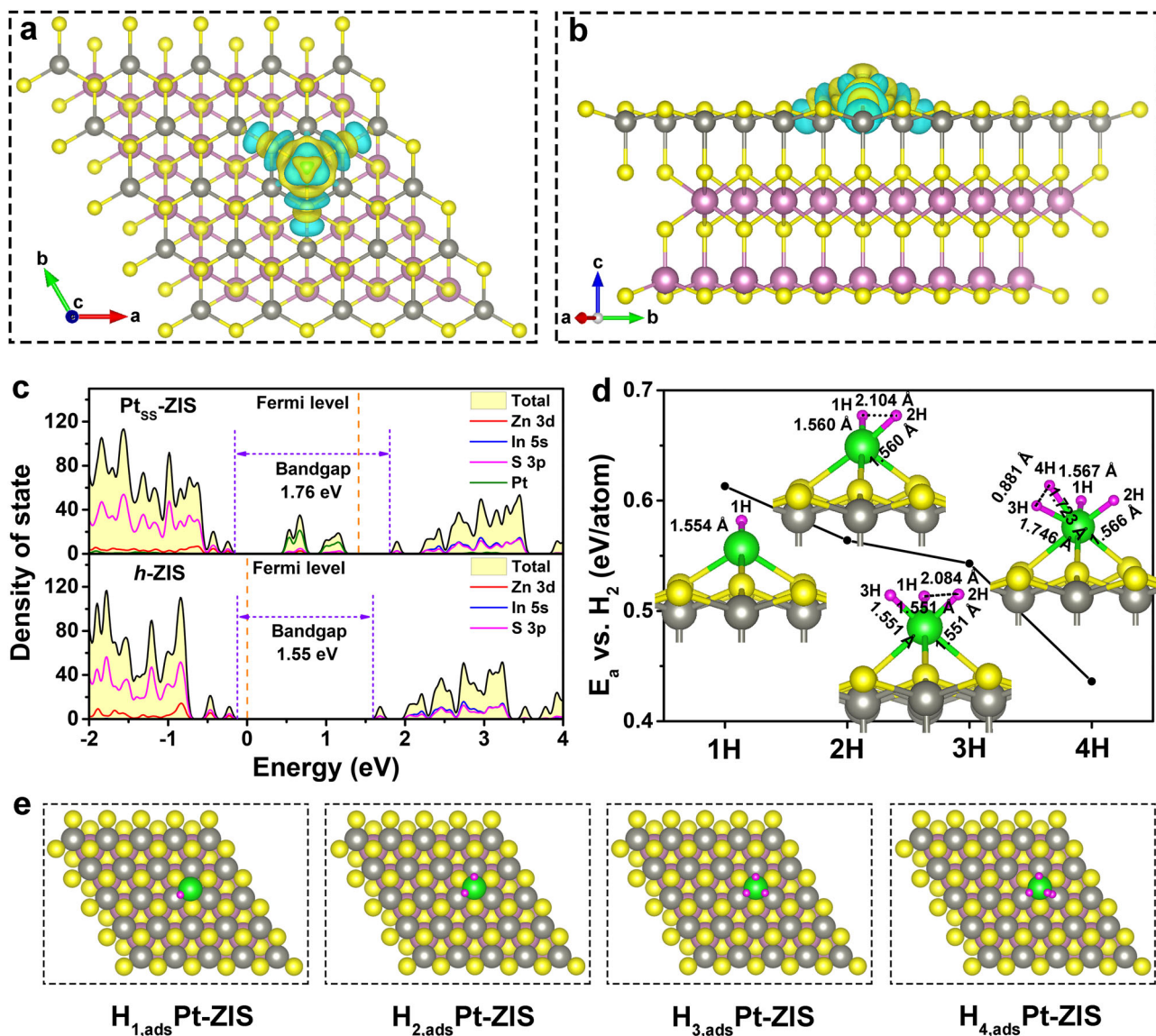


Fig. 5 Density functional theory (DFT) calculations. **a** Top and **b** side view of calculated charge difference surfaces of Pt₅₅-ZIS with yellow and cyan colors represent positive and negative electron density isosurfaces, respectively. The value of isosurface is 0.002e/bohr³. **c** Density of states of the *h*-ZIS and Pt₅₅-ZIS. **d** Calculated adsorption energies of H atoms as a function of the H coverages (from one H atom to four H atoms) on the single Pt atom photocatalysts with *h*-ZIS as support. The H-H and Pt-H distances are shown in the figure. The adsorption energies (E_a) were calculated by: $E_a = [E_{\text{Pt}_{55}\text{-ZIS}} + \frac{1}{2}E_{\text{H}_2} - E_{\text{Pt}_{55}\text{-ZIS+nH}}]/n$. The yellow, gray, pink, green, and purple spheres represent the S, Zn, In, Pt, and H atoms, respectively. **e** Side view of Pt₅₅-ZIS schematic structure with one H atom, two H atoms, three H atoms, and four H atoms chemisorbed on Pt atom, termed as H_{1,ads}-Pt-ZIS, H_{2,ads}-Pt-ZIS, H_{3,ads}-Pt-ZIS, and H_{4,ads}-Pt-ZIS, respectively.

protrusion-like single atoms could continuously enrich protons, which issues an improvement in proton mass transfer, thus boosting the kinetics of H₂ production on the Pt single atom^{22,26,50,52}. Active blocking experiment by introducing thiocyanate ion (SCN⁻¹) into the catalyst system dictates a drastically decreased H₂ generation rate from 350.1 to 27.44 μmol h⁻¹ with the increase of KSCN concentration, confirming that Pt single atoms indeed serve as the centers for HER (Supplementary Fig. 46). Based on calculations, the adsorbed Pt single sites onto the surface of *h*-ZIS manifests a fast formation and release of molecular hydrogen, leading to an outstanding catalytic activity.

Discussion

By combining experimental results with theoretical calculations, the high catalytic performance of Pt_{0.3}-ZIS accompanied with long

durability is confirmed. The enhanced H₂ generation rate is due to the atomic protrusion-like Pt atoms with triple roles in the photocatalytic HER. First, single Pt atoms immobilized onto *h*-ZIS could tune the band structure of *h*-ZIS on upshifting the CBM, providing a larger reduction driving force. Second, the atomically dispersed Pt are acted as electron wells to accelerate charge separation and transportation. Third, the tridimensional protrusions induce effective proton mass transfer to the active Pt site and an almost thermoneutral ΔG_{H}^* for HER, which is also supported by the smallest overpotential of Pt_{0.3}-ZIS among *J-V* curves (Supplementary Fig. 47). A reasonable photocatalytic mechanism for HER from water is proposed (Supplementary Fig. 48). Upon light irradiation, the electron and hole pairs are generated and then migrate from the interior to the surface of *h*-ZIS. Due to the covalent Pt-S coordination bond, electrons are injected from the neighboring S atoms into Pt single atoms efficiently, followed by the reaction with

adsorbed protons to generate H₂. Simultaneously, the holes in *h*-ZIS are consumed by TEOA.

In summary, compared to the conventional defect-trapped-SSCs, atomically dispersed Pt sites are immobilized onto the basal plane of *h*-ZIS nanosheets to generate catalysts by a facile photochemical strategy. The efficient water reduction activity over Pt_{0.3}-ZIS proceeds via regulated band structure, improved charge separation, reduced H₂ evolution overpotential, and advanced protons mass transfer. The demonstration herein of constructing tridimensional protrusions through immobilizing ultralow content Pt SSCs onto 2D *h*-ZIS nanosheets presents a promising, cost- and energy-efficient avenue for boosting photocatalysis H₂ evolution, and this prototype potentially would stimulate innovative ideas of enabling future ambient HER catalysts of industrial interest. The phenomenon of triggering tip enhancement by high-curvature nano-textures could function as a general prescription to enhance the performances of catalysts achieved in other reactions, such as organic pollutants degradation, O₂ reduction, CO₂ reduction, and N₂ fixation.

Methods

Synthesis of hexagonal ZnIn₂S₄ (*h*-ZIS) nanosheets. In a typical synthesis, 68 mg ZnCl₂ (Aladdin, 99.95%), 293 mg InCl₃·4H₂O (Aladdin, 99.9%), and 300 mg trisodium citrate (Aladdin, 99.0%) are dissolved into 25 mL of deionized water and 5 mL of glycol (Shanghai LingFeng Chemical Reagent Co. LTD., AR). After being drastically stirred for 30 min at room temperature, 150 mg thioacetamide (TAA, SCR, AR) is then added into the solution. After another 30 min stirring, the heterogeneous solution was transferred into a 50 mL Teflon-lined stainless steel autoclave and maintained at 120 °C for 12 h in an oven. After natural cooling, the products were collected by centrifugation, rinsed two times with ethanol and distilled water, and then freeze-dried.

Synthesis of hexagonal ZnIn₂S₄ thin layers with S-vacancy (*h*-ZIS-V_S). The as-obtained *h*-ZIS (100 mg) was dissolved into 50 mL storage bottle containing 0.1 M NaBH₄ (Sinopharm Chemical ReagentCo., Ltd, AR). The mixture was heated at 60 °C in a water bath. After 5 min, the resultant dispersion was centrifuged, and then freeze-dried.

Synthesis of Pt-loaded *h*-ZIS and *h*-ZIS-V_S atomic layers (Pt-ZIS and Pt-ZIS-V_S). In a typical procedure of photochemical loading Pt on *h*-ZIS, 20 mg thin layers *h*-ZIS and different amounts of H₂PtCl₆ (4 mg mL⁻¹) were dispersed in an aqueous solution containing 45 mL H₂O and 5 mL triethanolamine (TEOA, XiLong Scientific, AR). Subsequently, the suspension is bubbled with argon gas through the reactor for 30 min to completely remove the dissolved oxygen and ensure that the reactor is in an anaerobic condition. The dispersion was kept stirring with a magnetic stirrer during visible light irradiation (λ > 420 nm). After the light treatment for 60 min, the sample was centrifuged and washed by deionized water twice and then freeze-dried. By alerting the volume of H₂PtCl₆ solution, the Pt content relative to *h*-ZIS was adjusted to about 0.1, 0.3, 0.7, 1.4, and 3.0 wt%, which were named as Pt_{0.1}-ZIS, Pt_{0.3}-ZIS, Pt_{0.7}-ZIS, Pt_{1.4}-ZIS, and Pt_{3.0}-ZIS, respectively. For the synthesis of Pt_{0.3}-ZIS-V_S, the procedure was similar to that of Pt_{0.3}-ZIS except changing *h*-ZIS to *h*-ZIS-V_S.

Preparation of Pt_{0.3}-ZIS thin films. Typically, Pt_{0.3}-ZIS (30 mg) powder was dispersed into ethanol (2 mL) and then sonicated for 10 min to obtain a colloidal solution. The film was prepared by drop-casting 400 μL of the colloidal solution onto roughened glass (1.5 × 2 cm²). Then the film was dried in a vacuum oven at the temperature of 60 °C.

Photocatalytic hydrogen production. Twenty milligrams of photocatalysts was dispersed in 45 mL aqueous solution containing 10 vol% TEOA using an ultrasonic bath. Subsequently, the suspension was bubbled with argon gas through the reactor for 30 min to completely remove the dissolved oxygen and ensure that the reactor was in an anaerobic condition. The samples were irradiated under visible light using a 300 W Xenon lamp for H₂ generation (PLS-SXE300D, Beijing Perfectlight Technology Co., Ltd, 300 mW cm⁻²). The reaction temperature is kept at about 8 °C. The visible light is filtered with a nominal 420 nm cutoff filter. The volume of H₂ was measured by Shimadzu GC-8A gas chromatograph equipped with an MS-5A column and thermal conductivity detector. The apparent quantum efficiency (AQE) was calculated using the following equation,

$$\text{AQE}(\%) = \frac{N_e}{N_p} \times 100\% = \frac{2 \times n_{\text{H}_2} \times N_A \times h \times c}{S \times P \times t \times \lambda} \times 100\% \quad (1)$$

where N_p is the total incident photons, N_e is the total reactive electrons, n_{H_2} is the amount of H₂ molecules, N_A is Avogadro constant, h is the Planck constant, c is the speed of light, S is the irradiation area, P is the intensity of irradiation light, t is the photoreaction time, and λ is the wavelength of the monochromatic light. For the stability test, the photocatalyst was continuously irradiated for 50 h. The turnover frequency (TOF) was calculated according to the following equation:

$$\text{TOF} = \frac{n_{(\text{H}_2)}}{n_{(\text{Pt})} \cdot \tau} \quad (2)$$

Data availability

All data relevant to this study are available from the corresponding author upon reasonable request. The source data are provided as a Source data file. Source data are provided with this paper.

Received: 20 May 2021; Accepted: 15 February 2022;

Published online: 11 March 2022

References

- Chen, X., Shen, S., Guo, L. & Mao, S. S. Semiconductor-based photocatalytic hydrogen generation. *Chem. Rev.* **110**, 6503–6570 (2010).
- Lei, Z. et al. Photocatalytic water reduction under visible light on a novel ZnIn₂S₄ catalyst synthesized by hydrothermal method. *Chem. Commun.* **17**, 2142–2143 (2003).
- Yang, M.-Q. et al. Self-surface charge exfoliation and electrostatically coordinated 2D hetero-layered hybrids. *Nat. Commun.* **8**, 14224 (2017).
- Yang, W. et al. Enhanced photoexcited carrier separation in oxygen-doped ZnIn₂S₄ nanosheets for hydrogen evolution. *Angew. Chem. Int. Ed.* **55**, 6716–6720 (2016).
- Wang, S., Guan, B. Y., Wang, X. & Lou, X. W. D. Formation of hierarchical Co₉S₈@ZnIn₂S₄ heterostructured cages as an efficient photocatalyst for hydrogen evolution. *J. Am. Chem. Soc.* **140**, 15145–15148 (2018).
- Shi, X. et al. Ultrathin ZnIn₂S₄ nanosheets with active (110) facet exposure and efficient charge separation for cocatalyst free photocatalytic hydrogen evolution. *Appl. Catal. B Environ.* **256**, 118616 (2020).
- Du, C. et al. Half-unit-cell ZnIn₂S₄ monolayer with sulfur vacancies for photocatalytic hydrogen evolution. *Appl. Catal. B Environ.* **248**, 193–201 (2019).
- Zhang, S. et al. MoS₂ quantum dot growth induced by S vacancies in a ZnIn₂S₄ monolayer: atomic-level heterostructure for photocatalytic hydrogen production. *ACS Nano* **12**, 751–758 (2018).
- Shi, X. et al. Inert basal plane activation of two-dimensional ZnIn₂S₄ via Ni atom doping for enhanced co-catalyst free photocatalytic hydrogen evolution. *J. Mater. Chem. A* **8**, 13376–13384 (2020).
- Luo, N. et al. Visible-light-driven coproduction of diesel precursors and hydrogen from lignocellulose-derived methylfurans. *Nat. Energy* **4**, 575–584 (2019).
- Chen, Y. et al. Selective recovery of precious metals through photocatalysis. *Nat. Sustain.* **4**, 618–626 (2021).
- Qi, K. et al. Single-atom cobalt array bound to distorted 1T MoS₂ with ensemble effect for hydrogen evolution catalysis. *Nat. Commun.* **10**, 5231 (2019).
- Huang, Y. et al. Atomically engineering activation sites onto metallic 1T-MoS₂ catalysts for enhanced electrochemical hydrogen evolution. *Nat. Commun.* **10**, 982 (2019).
- Chen, Y. et al. Single-atom catalysts: synthetic strategies and electrochemical applications. *Joule* **2**, 1242–1264 (2018).
- Wang, Y. et al. Catalysis with two-dimensional materials confining single atoms: concept, design, and applications. *Chem. Rev.* **119**, 1806–1854 (2019).
- Park, J. et al. Investigation of the support effect in atomically dispersed Pt on WO_{3-x} for utilization of Pt in the hydrogen evolution reaction. *Angew. Chem. Int. Ed.* **58**, 16038–16042 (2019).
- Yan, Q.-Q. et al. Reversing the charge transfer between platinum and sulfur-doped carbon support for electrocatalytic hydrogen evolution. *Nat. Commun.* **10**, 4977 (2019).
- Deng, J. et al. Triggering the electrocatalytic hydrogen evolution activity of the inert two-dimensional MoS₂ surface via single-atom metal doping. *Energy Environ. Sci.* **8**, 1594–1601 (2015).
- Fang, S. et al. Uncovering near-free platinum single-atom dynamics during electrochemical hydrogen evolution reaction. *Nat. Commun.* **11**, 1029 (2020).
- Zeng, Z. et al. Single-atom platinum confined by the interlayer nanospace of carbon nitride for efficient photocatalytic hydrogen evolution. *Nano Energy* **69**, 104409 (2020).

21. Zuo, Q. et al. Ultrathin metal–organic framework nanosheets with ultrahigh loading of single Pt atoms for efficient visible-light-driven photocatalytic H₂ evolution. *Angew. Chem. Int. Ed.* **58**, 10198–10203 (2019).
22. Liu, D. et al. Atomically dispersed platinum supported on curved carbon supports for efficient electrocatalytic hydrogen evolution. *Nat. Energy* **4**, 512–518 (2019).
23. Li, J. et al. Accelerated dinitrogen electroreduction to ammonia via interfacial polarization triggered by single-atom protrusions. *Chem* **6**, 885–901 (2020).
24. Liu, P. et al. Photochemical route for synthesizing atomically dispersed palladium catalysts. *Science* **352**, 797–800 (2016).
25. Hejazi, S. et al. On the controlled loading of single platinum atoms as a co-catalyst on TiO₂ anatase for optimized photocatalytic H₂ generation. *Adv. Mater.* **32**, 1908505 (2020).
26. Lau, T. H. M. et al. Engineering monolayer 1T-MoS₂ into a bifunctional electrocatalyst via sonochemical doping of isolated transition metal atoms. *ACS Catal.* **9**, 7527–7534 (2019).
27. Wu, X. et al. Surface step decoration of isolated atom as electron pumping: atomic-level insights into visible-light hydrogen evolution. *Nano Energy* **45**, 109–117 (2018).
28. Zhang, J. et al. Single platinum atoms immobilized on an MXene as an efficient catalyst for the hydrogen evolution reaction. *Nat. Catal.* **1**, 985–992 (2018).
29. Zhu, J. et al. Enhanced electrocatalytic hydrogen evolution activity in single-atom Pt-decorated VS₂ nanosheets. *ACS Nano* **14**, 5600–5608 (2020).
30. Jiang, K. et al. Single platinum atoms embedded in nanoporous cobalt selenide as electrocatalyst for accelerating hydrogen evolution reaction. *Nat. Commun.* **10**, 1743 (2019).
31. Wu, C. et al. Monoatomic platinum-anchored metallic MoS₂: correlation between surface dopant and hydrogen evolution. *J. Phys. Chem. Lett.* **10**, 6081–6087 (2019).
32. Guan, Y. et al. Ganoderma-like MoS₂/NiS₂ with single platinum atoms doping as an efficient and stable hydrogen evolution reaction catalyst. *Small* **14**, 1800697 (2018).
33. Qiao, B. et al. Single-atom catalysis of CO oxidation using Pt₁/FeO_x. *Nat. Chem.* **3**, 634–641 (2011).
34. Zhang, Z. et al. Thermally stable single atom Pt/m-Al₂O₃ for selective hydrogenation and CO oxidation. *Nat. Commun.* **8**, 16100 (2017).
35. Schröder, M. et al. Hydrogen evolution reaction in a large-scale reactor using a carbon nitride photocatalyst under natural sunlight irradiation. *Energy Technol.* **3**, 1014–1017 (2015).
36. Zhang, N. et al. Near-field dielectric scattering promotes optical absorption by platinum nanoparticles. *Nat. Photon* **10**, 473–482 (2016).
37. Di, J. et al. Isolated single atom cobalt in Bi₃O₅Br atomic layers to trigger efficient CO₂ photoreduction. *Nat. Commun.* **10**, 2840 (2019).
38. Xiao, X. et al. A promoted charge separation/transfer system from Cu single atoms and C₃N₄ layers for efficient photocatalysis. *Adv. Mater.* **32**, 2003082 (2020).
39. Zhu, M. et al. Metal-free photocatalyst for H₂ evolution in visible to near-infrared region: black phosphorus/graphitic carbon nitride. *J. Am. Chem. Soc.* **139**, 13234–13242 (2017).
40. Zhu, M., Sun, Z., Fujitsuka, M. & Majima, T. Z-Scheme photocatalytic water splitting on a 2D heterostructure of black phosphorus/bismuth vanadate using visible light. *Angew. Chem. Int. Ed.* **57**, 2160–2164 (2018).
41. Gao, S. et al. Highly efficient and exceptionally durable CO₂ photoreduction to methanol over freestanding defective single-unit-cell bismuth vanadate layers. *J. Am. Chem. Soc.* **139**, 3438–3445 (2017).
42. Wang, S., Guan, B. Y. & Lou, X. W. D. Construction of ZnIn₂S₄–In₂O₃ hierarchical tubular heterostructures for efficient CO₂ photoreduction. *J. Am. Chem. Soc.* **140**, 5037–5040 (2018).
43. Židek, K. et al. Ultrafast dynamics of multiple exciton harvesting in the CdSe–ZnO system: electron injection versus Auger recombination. *Nano Lett.* **12**, 6393–6399 (2012).
44. Abdellah, M. et al. Balancing electron transfer and surface passivation in gradient CdSe/ZnS core–shell quantum dots attached to ZnO. *J. Phys. Chem. Lett.* **4**, 1760–1765 (2013).
45. Wang, W.-K. et al. Single-molecule and -particle probing crystal edge/corner as highly efficient photocatalytic sites on a single TiO₂ particle. *Proc. Natl Acad. Sci. USA* **116**, 18827–18833 (2019).
46. Jiang, W. et al. Consciously constructing heterojunction or direct Z-scheme photocatalysts by regulating electron flow direction. *ACS Catal.* **8**, 2209–2217 (2018).
47. Zhao, Q. et al. Single nickel atoms anchored on nitrogen-doped graphene as a highly active cocatalyst for photocatalytic H₂ evolution. *ACS Catal.* **8**, 11863–11874 (2018).
48. Tian, B. et al. Supported black phosphorus nanosheets as hydrogen-evolving photocatalyst achieving 5.4% energy conversion efficiency at 353 K. *Nat. Commun.* **9**, 1397 (2018).
49. Wang, P. et al. Atomic insights for optimum and excess doping in photocatalysis: a case study of few-layer Cu–ZnIn₂S₄. *Adv. Funct. Mater.* **29**, 1807013 (2019).
50. Cheng, N. et al. Platinum single-atom and cluster catalysis of the hydrogen evolution reaction. *Nat. Commun.* **7**, 13638 (2016).
51. Hinnemann, B. et al. Biomimetic hydrogen evolution: MoS₂ nanoparticles as catalyst for hydrogen evolution. *J. Am. Chem. Soc.* **127**, 5308–5309 (2005).
52. Liu, M. et al. Enhanced electrocatalytic CO₂ reduction via field-induced reagent concentration. *Nature* **537**, 382–386 (2016).

Acknowledgements

This work is supported by the National Natural Science Foundation of China (Nos. 21902143 and 51702287), Natural Science Foundation of Zhejiang Province (No. LY21B030005), Guangdong Basic and Applied Basic Research Foundation (No. 2020B1515020038), and the Natural Science Foundation of Jiangsu Province (No. BK20190640). M.Z. thanks the Pearl River Talent Recruitment Program of Guangdong Province (2019QN01L148). We thank the Taiwan National Synchrotron Radiation Research Center for XAFS measurement.

Author contributions

X.S. and M.Z. constructed and planned the whole project. X.S., C.D., and X.W. performed the synthesis, characterization, and photocatalysis. X.S. and C.D. performed the XAS in terms of XANES and EXAFS tests. X.W. performed the in situ FTIR tests. J.H. performed the photodegradation and photo-electrochemical experiments. L.M. and J.Z. conducted the DFT calculations. X.S. and L.M. writing—original draft, M.Z., L.Z., and H.Z. writing—review and editing. All authors analyzed the data and commented on the manuscript.

Competing interests

The authors declare no competing interests.

Additional information

Supplementary information The online version contains supplementary material available at <https://doi.org/10.1038/s41467-022-28995-1>.

Correspondence and requests for materials should be addressed to Liang Mao, Huajun Zheng or Mingshan Zhu.

Peer review information *Nature Communications* thanks Kyu Hyoung Lee and the other, anonymous, reviewers for their contribution to the peer review of this work.

Reprints and permission information is available at <http://www.nature.com/reprints>

Publisher's note Springer Nature remains neutral with regard to jurisdictional claims in published maps and institutional affiliations.



Open Access This article is licensed under a Creative Commons Attribution 4.0 International License, which permits use, sharing, adaptation, distribution and reproduction in any medium or format, as long as you give appropriate credit to the original author(s) and the source, provide a link to the Creative Commons license, and indicate if changes were made. The images or other third party material in this article are included in the article's Creative Commons license, unless indicated otherwise in a credit line to the material. If material is not included in the article's Creative Commons license and your intended use is not permitted by statutory regulation or exceeds the permitted use, you will need to obtain permission directly from the copyright holder. To view a copy of this license, visit <http://creativecommons.org/licenses/by/4.0/>.

© The Author(s) 2022